14th International Symposium on Turbulence and Shear Flow Phenomena (TSFP14)
Heidelberg, Germany, July 28–31, 2026

SPECTRAL ANALYSIS OF TURBULENT TRANSPORT OF REYNOLDS STRESSES IN ELLIPTICAL PIPE FLOWS

Taylor C. Opperman, Bing-Chen Wang
Department of Mechanical Engineering
University of Manitoba
Winnipeg, MB, R3T 5V6, Canada
oppermat@myumanitoba.ca, BingChen.Wang@umanitoba.ca

ABSTRACT

Turbulent transport of Reynolds normal stresses in elliptical pipe flows at two Reynolds numbers (of $Re_\tau = 180$ and 395) has been studied using direct numerical simulations (DNS) in both physical and spectral spaces. Owing to the varying curvature along the periphery of the elliptical pipe, the strength of the transport terms of the Reynolds normal stresses increases significantly along the semi-major axis as the Reynolds number increases. The budgets are dominated by turbulence production, balanced by turbulent diffusion, viscous diffusion, and viscous dissipation. In spectral space it is interesting to observe that the modal values of all budget terms of the streamwise premultiplied velocity spectra show a noticeable shift towards smaller wavelengths as the Reynolds number increases.

INTRODUCTION

The wall curvature of an elliptical pipe varies azimuthally, with its maximum and minimum occurring at the ends of the major and minor axes, respectively. This varying curvature fosters large-scale secondary motions in the cross-stream direction, which have a significant impact on the statistical moments and coherent structures of the flow.

Cain & Duffy (1971) investigated the mean characteristics of turbulent flow confined within elliptical pipes of aspect ratios $AR = 1.5{:}1$ and 2:1 for a wide range of Reynolds numbers. They observed that the wall shear stress varied substantially along the azimuthal direction, independent of both Reynolds number and aspect ratio. Nikitin & Yakhot (2005) performed DNS to study elliptical pipe flow at a fixed bulk Reynolds number of $Re_{D_h} = 6000$ with a pipe length of $L_z = 6D_h$. Four counter-rotating vortical structures resulting from the azimuthal variation of wall-tangent and wall-normal Reynolds stresses were observed in the cross-stream directions. They also observed that the turbulence kinetic energy (TKE) was lower near the two ends of the major axis due to the turbulence-suppressing effects of transverse wall curvature. Voronova & Nikitin (2006) and Voronova & Nikitin (2007) conducted DNS of turbulent elliptical pipe flows of $AR = 2{:}1$ at $Re_{D_h} = 4000$ and 6000. They determined that the distribution and intensity of secondary flows are mainly caused by differences between the radial and azimuthal Reynolds normal stresses in the near-wall region of the elliptical pipe. Recently, Rosas *et al.* (2021) and Rosas & Wang (2022) performed DNS to study the impact of radial system rotation on turbulent flow and heat transfer in an elliptical pipe. The effects of Coriolis forces on the statistical moments of the velocity and temperature fields were thoroughly investigated. Opperman *et al.* (2025) performed DNS to investigate turbulent flows within elliptical pipes of varying aspect ratios. They observed that as a result of the varying wall curvature of elliptical pipes, large-scale secondary flows appear in the cross-stream direction as two pairs of counter-rotating vortices at relatively small AR values, which significantly impact the turbulence statistics of the flow.

In his pioneering work, Lumley (1964) derived the spectral energy equation to study the budget balance of TKE in the spectral space in the context of wall turbulence. Mizuno (2016) performed DNS to study the inter-scale and wall-normal transport of TKE in turbulent channel flows, and showed that the fluctuating flow structures responsible for transporting TKE across different scales were self-similar. Lee & Moser (2019) conducted a spectral analysis of the budget balance of Reynolds stresses using DNS data of turbulent plane-channel flows, and observed that the large-scale streamwise-elongated flow structures played a significant role in the energy transport process. Yang *et al.* (2020) conducted DNS of a streamwise-rotating channel flow to study the sustaining mechanisms of Taylor-Götler-like (TGL) vortices, which appear as two layers of streamwise-elongated roll cells under fast system rotation. They observed that the large-scale TGL vortices absorbed energy from small-scale eddies through an inverse inter-scale energy transfer process. Xiong *et al.* (2025) performed a spectral analysis of TKE transport processes in turbulent flow through a channel roughened with circular-arc ribs. It was observed that the transport of TKE from moderate-scale wavelengths to small- and large-scale wavelengths occurred simultaneously within the internal shear layer caused by the rib crest. The transport of energy from moderate- to large-scale turbulent motions (i.e., the inverse energy transport) weakened as the Reynolds number increased. Kawata & Alfredsson (2018) conducted spectral analysis of turbulent transport of Reynolds stress in a plane-channel Couette flow. They observed that small-scale structures played an increasingly crucial role in sustaining turbulence energy production at large scales as the Reynolds number increases.

Notwithstanding the contributions reviewed above, the number of studies on spectral analysis of turbulent energy transport processes is still relatively limited in the current literature, primarily focusing on DNS of smooth-wall flows (Mizuno, 2016; Lee & Moser, 2019; Yang *et al.*, 2020) over the recent decade. To date, a study of the turbulent transport of velocity-spectrum tensor in elliptical pipe flows is still lacking.

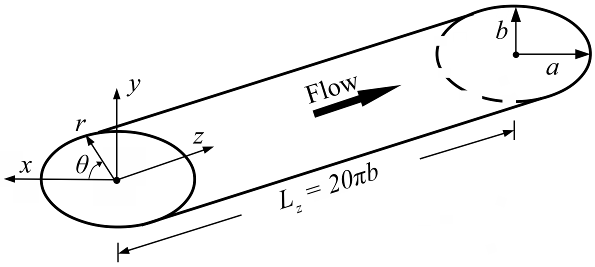

Figure 1: Computational domain and coordinate system of an elliptical pipe flow. Here, a and b denote the semi-major and semi-minor axes, respectively.

In view of this knowledge gap, the objective of this research is to conduct a detailed DNS study of turbulent transport of Reynolds stresses in elliptical pipe flows in both physical and spectral spaces.

Table 1: Key flow parameters and grid resolutions for the four test cases of varying AR values.

Re_τ (nominal)	180	395
Re_τ (actual)	179.92	395.11
Re_{D_h} (actual)	5329	12968
a/b	2	2
N_T (millions)	63.2	295.7
N_z	960	1296
L_z/b	20π	12π
L_z^+	8720	11481
Δz^+	9.1	8.9
Δn^+ (min − max)	0.2-3.4	0.2-4.0
$\bar{\Delta}/\eta$ (min-max)	0.49-1.91	0.62-2.65
LETOTs	122.3	61.2

TEST CASE AND NUMERICAL ALGORITHM

Figure 1 shows the geometry and coordinate system of a smooth elliptical pipe. The axial domain length has been set to $L_z = 20\pi b$, which is among the longest in the current literature of DNS of elliptical pipe flows (in order to fully capture the axially elongated turbulence structures). The incompressible flows are fully developed in the axial direction and are governed by the following equations:

$$\frac{\partial u_i}{\partial x_i} = 0 \quad , \tag{1}$$

$$\frac{\partial u_i}{\partial t} + u_j \frac{\partial u_i}{\partial x_j} = -\frac{1}{\rho}\Pi\delta_{i3} - \frac{1}{\rho}\frac{\partial p}{\partial x_i} + \nu \frac{\partial^2 u_i}{\partial x_j^2} \quad , \tag{2}$$

where the density and pressure of the fluid are denoted by ρ and p, respectively, while Π denotes the constant mean axial pressure gradient that drives the flow, and δ_{ij} is the Kronecker delta. With tensor notation, coordinates (x, y, z) and velocities (u, v, w) correspond to (x_1, x_2, x_3) and (u_1, u_2, u_3), respectively. A periodic boundary condition is applied to the streamwise direction along with a no-slip boundary condition enforced at the wall.

Two test cases (with $Re_\tau = 180$ and 395) of the elliptical-pipe flow are examined in our comparative study to investigate the effects of Reynolds number on turbulent transport of Reynolds stresses. The Reynolds number is defined as $Re_\tau = u_\tau R_h/\nu$. Here, $R_h = D_h/2$ is the hydraulic radius (or, one half the hydraulic diameter D_h) of an elliptical pipe and u_τ is the wall velocity determined by the average wall shear stress $\tau_{w,a}$ along the periphery of the elliptical pipe (i.e., $u_{\tau,a} = \sqrt{\tau_{w,a}/\rho}$). The aspect ratio of the pipe is held constant at $AR = 2:1$ for both test cases.

The governing equations were solved using the spectral-element code "Semtex", developed by Blackburn *et al.* (2019), which provides spectral accuracy suitable for conducting rigorous DNS. The code is written in C++ and Fortran programming languages and is made parallel using message passing interface (MPI) libraries. Time integration is performed using a second-order, three-step time-splitting scheme (Karniadakis *et al.*, 1991; Karniadakis & Sherwin, 2005). This code has been used by our group for conducting DNS studies of turbulent flow and heat transfer in channels roughened with circular-arc ribs (Xiong *et al.*, 2023, 2024, 2025), turbulent flow and heat convection in stationary and axially rotating elliptical and circular pipes (Rosas *et al.*, 2021; Rosas & Wang, 2022; Opperman *et al.*, 2025; Zhang & Wang, 2025), and turbulent flow in a square duct roughened by longitudinal ribs (Tachie *et al.*, 2025). The cross-section of the pipe is discretized into a finite-element mesh that is further discretized using an 8th-order Gauss-Lobatto-Legendre-Lagrange (GLLL) polynomial. In the streamwise (z) direction, all physical quantities are discretized in the spectral space based on Fourier expansions, with into 960 and 1296 modes used for the cases of $Re_\tau = 180$ and 395, respectively. Consequently, the total number of grid points is $N_T = 63.2$ to 295.7 million for the low and high Reynolds number flow cases, respectively. The grid spacing in the axial direction is uniform within a range of $\Delta z^+ = 9.1$-8.9 for cases of $Re_\tau = 180$ and 395, respectively. To ensure a precise calculation of the wall shear stress, the wall-normal distance of the first node off the wall is kept at $\Delta n^+ \leq 0.2$ for both cases. To confirm that the grid resolution is sufficiently fine for capturing the smallest turbulence scales in DNS, the ratio of the grid size ($\bar{\Delta} = \sqrt[3]{\Delta x \cdot \Delta y \cdot \Delta z}$) over the local Kolmogorov length scale (η) is examined, which varies within the range of $0.49 \leq \bar{\Delta}/\eta \leq 2.65$ in the cases of $Re_\tau = 180$ and 395. Here, the Kolmogorov length scale is defined as $\eta = (\nu^3/\varepsilon_k)^{1/4}$, and ε_k is the TKE dissipation rate. Table 1 summarizes the flow parameters and grid resolutions.

In the results analysis, the instantaneous velocity is decomposed as $u = \langle u \rangle + u'$, where a pair of angular brackets $\langle \cdot \rangle$ represents variables averaged over time and the homogeneous streamwise direction, and a prime symbol $(\cdot)'$ represents fluctuations from the mean. Variables expressed in wall coordinates denoted by superscript '+' were obtained using the wall friction velocity u_τ. For each simulation, 450 instantaneous snapshots were generated over 122.3 and 61.2 large-eddy turnover times (LETOTs) for the cases of $Re_\tau = 180$ and 395, respectively, resulting in 12.0 TB of data in total.

RESULTS AND DISCUSSION

Figure 2 compares the cross-sectional contours of the non-dimensionalized instantaneous streamwise velocity w^+ for both Reynolds number test cases. Both cases show the so-called "mushroom patterns" typical of a pipe flow. Figure 2(b) demonstrates an enhanced distribution of high-momentum fluid into the near-wall region at the ends of the major-axis as the Reynolds number increases from $Re_\tau = 180$ to 395.

Figure 3 compares the contours of the non-dimensionalized TKE (defined as $k^+ = \langle u_i' u_i' \rangle / 2u_\tau^2$) for both cases. The contours reveal that the TKE is concentrated

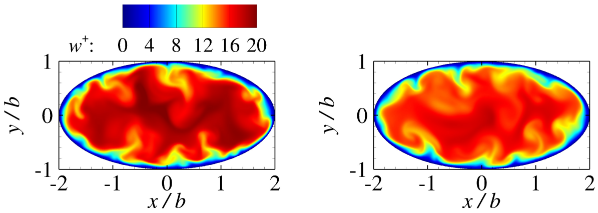

(a) $Re_\tau = 180$ (b) $Re_\tau = 395$

Figure 2: Contours of instantaneous velocity w^+ in the cross-stream plane corresponding to $z/L_z = 0.5$ at the final time step for each case.

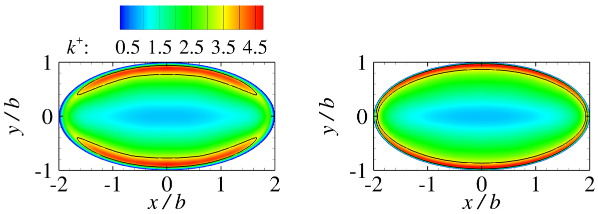

(a) $Re_\tau = 180$ (b) $Re_\tau = 395$

Figure 3: Contours of the non-dimensionalized TKE k^+. The black isopleths correspond to the value of $0.75(k^+)_{\max}$.

near the wall, with a maximum occurring at the ends of the minor axis in both cases. Furthermore, strong dampening of TKE is observed along the ends of the major axis for the lower Reynolds number test case. Interestingly, as the Reynolds number increases, the concentration of large TKE values migrates closer to the walls while becoming more uniformly distributed around the periphery of the elliptical pipe. This is clearly shown by the black isopleths in Fig. 3, which correspond to the value of $0.75(k^+)_{\max}$ for each test case.

Figure 4 presents the profiles of the non-dimensionalized Reynolds normal stresses along the semi-major axis for both test cases. Specifically, Fig. 4(a) presents the profiles of the streamwise component $\langle w'w'\rangle^+$, while Fig. 4(b) presents those of the cross-stream components $\langle u'u'\rangle^+$ and $\langle v'v'\rangle^+$. A comparison of Figs. 4(a) and (b) reveals that the peak values of all three components increase in magnitude as the Reynolds number increases. The peak value of $\langle w'w'\rangle^+$ migrates towards the end of the major axis slightly from a wall-normal distance of $x^+ = 16.7$ to 15.4 as the Reynolds number increases. The cross-stream components ($\langle u'u'\rangle^+$ and $\langle v'v'\rangle^+$) behave in a similar, yet more exaggerated manner. This suggests that the increase in TKE at the ends of the major axis observed in Fig. 3 results from two simultaneous trends as the Reynolds number increases. First, the turbulent motions of all three velocity components are increasing along the semi-major axis. Second, the largest cross-stream velocity fluctuations shift closer to the end of the semi-major axis.

The budget balance of the Reynolds stress transport equations for a steady state flow can be written as

$$\frac{\partial \langle u_i'u_j'\rangle}{\partial t} = H_{ij} + P_{ij} + \Pi_{ij} + \varepsilon_{ij} + D_{ij}^t + D_{ij}^p + D_{ij}^v = 0 \quad , \qquad (3)$$

where H_{ij}, P_{ij}, Π_{ij}, ε_{ij}, D_{ij}^t, D_{ij}^p, and D_{ij}^v are the convection, turbulent production, pressure-strain, viscous dissipation, turbulent diffusion, pressure diffusion, and viscous diffusion terms, respectively. The definitions of these budget terms are presented in Appendix A.

Figure 5 compares the budget balances of the three Reynolds normal stresses ($\langle u'u'\rangle^+$, $\langle v'v'\rangle^+$ and $\langle w'w'\rangle^+$) along the semi-major axis for the cases of $Re_\tau = 180$ and 395. All terms have been non-dimensionalized by u_τ^4/ν. Clearly, the

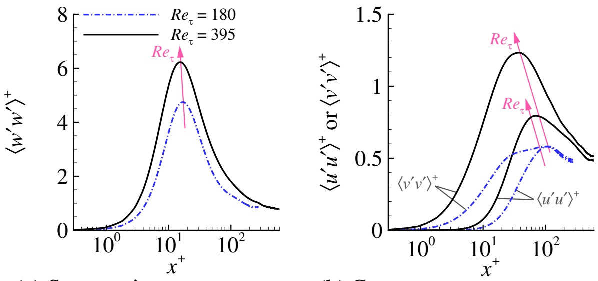

(a) Streamwise component (b) Cross-stream components

Figure 4: Profiles of the non-dimensionalized Reynolds normal stresses $\langle u_i'u_j'\rangle^+$ along the semi-major axis. Pink arrows point in the direction of an increasing Reynolds number.

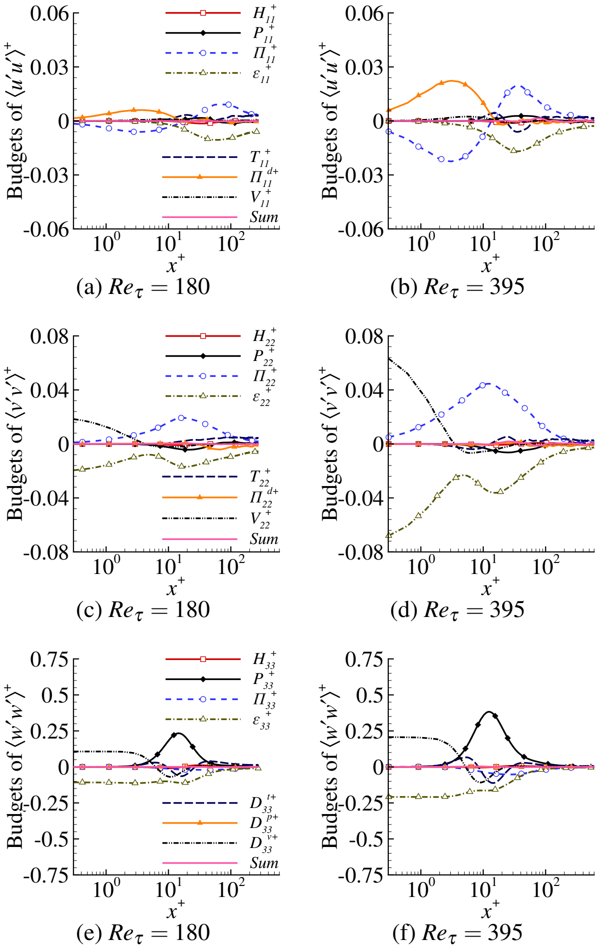

(a) $Re_\tau = 180$ (b) $Re_\tau = 395$

(c) $Re_\tau = 180$ (d) $Re_\tau = 395$

(e) $Re_\tau = 180$ (f) $Re_\tau = 395$

Figure 5: Profiles of the budget terms of Reynolds normal stresses ($\langle u'u'\rangle^+$, $\langle v'v'\rangle^+$ and $\langle w'w'\rangle^+$) along the semi-major axis. All terms are non-dimensionalized by u_τ^4/ν.

magnitudes of $\langle u'u'\rangle^+$ and $\langle v'v'\rangle^+$ are significantly reduced compared with those of $\langle w'w'\rangle^+$. In Figs. 5(a) and (b), it is shown that the budget of $\langle u'u'\rangle$ is balanced by the pressure-strain Π_{11}^+ and pressure diffusion D_{11}^{v+} acting as source and sink terms, respectively, in the near-wall region. Further from the wall, for $x^+ > 10$, the budget is balanced by the pressure diffusion D_{11}^{v+} and viscous dissipation ε_{11}^+ acting as source and sink terms, respectively. In Figs. 5(c) and (d), it is observed that the budget is balanced by the pressure-strain Π_{22}^+ acting as a source term and the viscous dissipation ε_{22}^+ acting as a sink term for both test cases. In the near-wall region, for $x^+ < 2$, the budget is balanced by viscous diffusion D_{22}^{v+} and viscous dissipation ε_{22}^+ acting as source and sink terms, respectively. From Figs. 5(e) and (f), the viscous diffusion D_{33}^{v+} and dissipa-

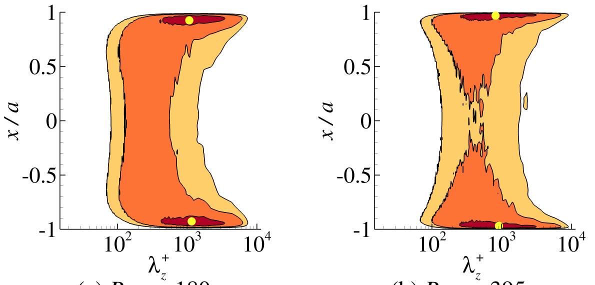

(a) $Re_\tau = 180$ (b) $Re_\tau = 395$

Figure 6: Contour plots of the normalized 1-D energy spectrum $k_z^+\phi_k^+/(k_z\phi_k)_{\max}$ displayed with respect to non-dimensionalized streamwise wavelength λ_z^+ extracted at the central horizontal plane through the major axis. The yellow dot indicates the peak value of $k_z^+\phi_k^+/(k_z\phi_k)_{\max}$. Three contour levels of the energy spectrum of plotted, with the innermost, intermediate and outermost isopleths corresponding to 62.5%, 25% and 12.5% of the peak value, respectively.

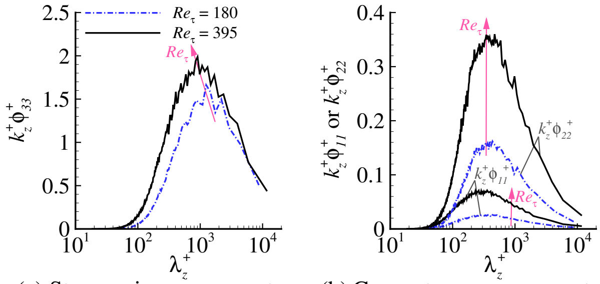

(a) Streamwise component (b) Cross-stream components

Figure 7: Profiles of the non-dimensionalized premultiplied velocity spectra $k_z^+\phi_{ij}^+$ calculated at the peak position of $\langle w'w'\rangle^+$ along the semi-major axis for each test case (i.e, at a distance from the wall of $x^+ = 16.7$ and 15.4 for the cases of $Re_\tau = 180$ and 395, respectively). Pink arrows point in the direction of an increasing Reynolds number.

tion ε_{33}^+ dominate the budget close to the wall. Meanwhile, P_{33}^+ acts as the dominant source term balanced by the sink terms of turbulent diffusion D_{33}^{t+}, viscous diffusion D_{33}^{v+}, and dissipation ε_{33}^+ near the pipe center. It is worth noting that the sign of the pressure-strain term Π_{33}^+ is opposite that of Π_{22}^+, demonstrating the role of the pressure-strain term in the redistribution of energy between streamwise and cross-stream fluctuations at the end of the semi-major axis.

Owing to the streamwise homogeneity of the elliptical pipe flow, the premultiplied velocity spectra $k_z^+\phi_{ij}^+$ can be a useful tool for analyzing the characteristic streamwise length scales of turbulence structures. Here, $\phi_{ij} = \mathrm{Re}\{\overline{\widehat{u_i'}^{*}\widehat{u_j'}}\}$ is the velocity-spectrum tensor, where $\mathrm{Re}\{\cdot\}$ denotes the real part of the solution, and an overline $\overline{(\cdot)}$ denotes averaging over time. Additionally, superscript '$*$' denotes the complex conjugate and a hat symbol $\widehat{(\cdot)}$ indicates the Fourier transform in the streamwise (z) direction of a velocity fluctuation component. Specifically,

$$\widehat{u_i'}(x,y,k_z,t) = \frac{1}{L_z}\int_0^{L_z} u_i'(x,y,k_z,t)e^{-\mathrm{I}k_z z}dz \quad . \tag{4}$$

Here, $\mathrm{I} = \sqrt{-1}$ is the imaginary unit, and $k_z = n_z k_{z0}$ is the streamwise wavenumber, $n_z \in [-N_z/2, N_z/2-1]$ is an integer, and $k_{z0} = 2\pi/L_z$ is the smallest positive wavenumber. The streamwise wavelength is given by $\lambda_z = 2\pi/k_z$.

Figure 6 displays the isopleths of the 1-D premultiplied energy spectra $k_z^+\phi_k^+$ of TKE, where $\phi_k = \phi_{ii}/2$. The yellow dot demarcates the location of the maximum value (i.e., $(k_z\phi_k)_{\max}$). Each contour was extracted along the major axis in the x/a-λ_z^+ plane and has been normalized by $(k_z\phi_k)_{\max}$ of their respective test case. The three isopleth levels are defined by 62.5%, 25% and 12.5% of $(k_z\phi_k)_{\max}$. The maximum energy occurs at the positions of $(x/a,\ \lambda_z^+) \approx (0.935,\ 1200)$ and $(0.975,\ 875)$ for the low and high Reynolds number test cases, respectively. Clearly, the most energetic eddies decrease in wavelength and shift towards the wall as the Reynolds number increases. This is in agreement with the TKE contours and Reynolds normal stress profiles observed in Figs. 3 and 4, respectively, which showed a migration towards the wall of enhanced energetic motions. Importantly, the isopleths are fully contained within the domain for both test cases, indicating that the most energetically relevant turbulence motions have been well captured by the DNS.

Figure 7 compares the profiles of the premultiplied streamwise, spanwise, and vertical velocity spectra ($k_z^+\phi_{33}^+$, $k_z^+\phi_{11}^+$ and $k_z^+\phi_{22}^+$, respectively) at the location of maximum $\langle w'w'\rangle^+$ along the semi-major axis for each test case. It is observed that the magnitudes of all three components increase as the Reynolds number increases from $Re_\tau = 180$ to 395. Additionally, it is seen that the peak positions of all three components shift towards smaller wavelengths as the Reynolds number increases. Specifically, the characteristic wavelengths (i.e., the modal wavelength corresponding to $(k_z^+\phi_{ij}^+)_{\max}$) shift from $\lambda_z^+ = 370$ to 350, 400 to 350, and 1250 to 885 for $k_z^+\phi_{11}^+$, $k_z^+\phi_{22}^+$ and $k_z^+\phi_{33}^+$, respectively, as the Reynolds number increases. From Fig. 7(b), it is interesting to observe that characteristic wavelengths corresponding to peaks of $k_z^+\phi_{11}^+$ and $k_z^+\phi_{22}^+$ are less sensitive to changes in Reynolds number. From Fig. 6(a), it is observed that the profile of $k_z^+\phi_{33}^+$ is most sensitive to changes in Reynolds number for wavelengths $\lambda_z^+ < 2000$.

In order to gain a deeper understanding of the various scales involved in the transport of Reynolds normal stresses, the transport equations of the velocity-spectrum tensor can be examined, which reads in Fourier space as

$$\frac{\partial\overline{\widehat{u_i'}^{*}\widehat{u_j'}}}{\partial t} = \widetilde{H}_{ij} + \widetilde{P}_{ij} + \widetilde{T}_{ij} + \widetilde{\Pi}_{ij} + \widetilde{\varepsilon}_{ij} + \widetilde{D}_{ij}^{t} + \widetilde{D}_{ij}^{p} + \widetilde{D}_{ij}^{v} = 0 \quad , \tag{5}$$

where $\widetilde{H}_{ij}$, $\widetilde{P}_{ij}$, $\widetilde{T}_{ij}$, $\widetilde{\Pi}_{ij}$, $\widetilde{\varepsilon}_{ij}$, $\widetilde{D}_{ij}^{t}$, $\widetilde{D}_{ij}^{p}$, and $\widetilde{D}_{ij}^{v}$ are the convection, turbulent production, inter-scale transport, pressure-strain, viscous dissipation, turbulent diffusion, pressure diffusion, and viscous diffusion terms, respectively. The definitions of these budget terms are given in Appendix B. It is worth noting that the integral of the inter-scale transport term $\widetilde{T}_{ij}$ over the spectral space is equal to zero, indicating that the energy transported by $\widetilde{T}_{ij}$ is strictly between turbulent motions of different wavelengths.

Figure 8 shows the budget balances of the three components of the premultiplied velocity-spectrum tensor associated with the Reynolds normal stresses at the location of maximum $\langle w'w'\rangle^+$ along the semi-major axis for each case. All budget terms have been plotted against the non-dimensional streamwise wavelength $\lambda_z^+ = \lambda_z u_\tau/\nu$. Clearly, the magnitudes of budget terms for $k_z^+\phi_{11}^+$ and $k_z^+\phi_{22}^+$ are significantly smaller than those for $k_z^+\phi_{33}^+$, even as the Reynolds number increases. Figures 8(c) and (d) show that the budget balance of $k_z^+\phi_{22}^+$ is dominated by the pressure-strain term $k_z^+\widetilde{\Pi}_{22}^+$, which acts as a source, while viscous dissipation term $k_z^+\widetilde{\varepsilon}_{22}^+$ acts as the primary sink. Interestingly, the inter-scale transport term $k_z^+\widetilde{T}_{22}^+$ acts as a sink for wavelengths below $\lambda_z^+ \approx 400$ and as a source for wavelengths above this value. From this, it is understood that $k_z^+\widetilde{T}_{22}^+$ plays an important role in the inverse transport of energy from small to large scales. Figures 8(e) and (f) reveal that the balance of the premultiplied streamwise velocity spectrum $k_z^+\phi_{33}^+$ is dominated by the turbulent production term $k_z^+\widetilde{P}_{33}^+$, which acts as a source, while viscous dissipation $k_z^+\widetilde{\varepsilon}_{33}^+$ and turbulent diffusion $k_z^+\widetilde{D}_{33}^{t+}$ act as the dominant sink terms. The signs of $k_z^+\widetilde{\Pi}_{33}^+$ and $k_z^+\widetilde{T}_{33}^+$ are opposite to those of their counterparts in the $k_z^+\phi_{22}^+$ budget for both test cases. This is consistent with the observations of Fig. 5, indicating a redistribution of TKE between the streamwise and vertical Reynolds normal-stress components at the end of the semi-major axis. In contrast to its vertical cross-stream counterpart, the inter-scale transport term $k_z^+\widetilde{T}_{33}^+$ plays an important role in the transfer of energy from large to small scales. The characteristic wavelengths of all transport terms in the $k_z^+\phi_{33}^+$ budget decrease as the Reynolds number increases. In particular, the characteristic wavelength of the negative peak of $k_z^+\widetilde{T}_{33}^+$ remains nearly constant at $\lambda_z^+ \approx 190$, whereas that of the positive peak decreases from $\lambda_z^+ = 1700$ to 1150 with increasing Reynolds number. Likewise, the characteristic wavelength of viscous diffusion, $k_z^+\widetilde{D}_{33}^{\nu+}$, remains approximately constant at $\lambda_z^+ \approx 1200$ for both Reynolds number test cases.

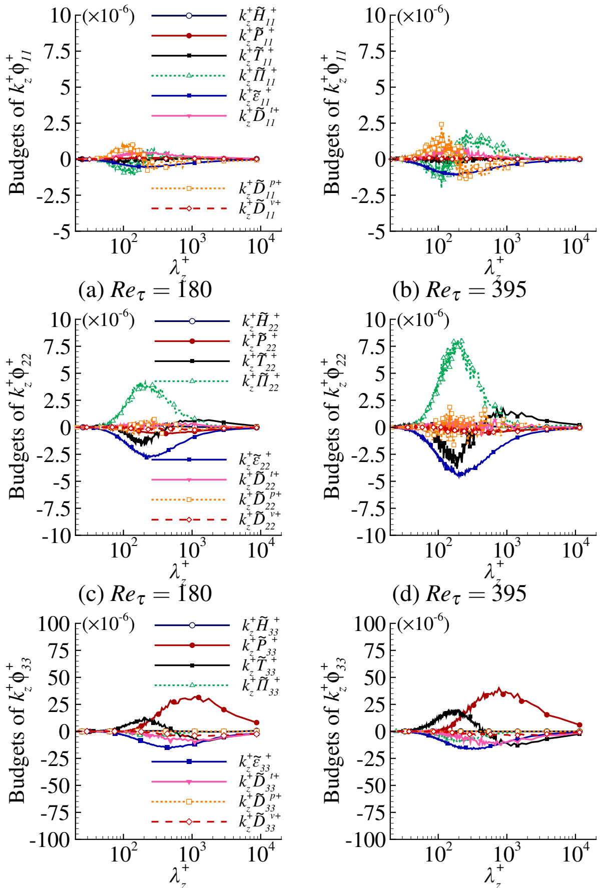

(a) $Re_\tau = 180$ (b) $Re_\tau = 395$

(c) $Re_\tau = 180$ (d) $Re_\tau = 395$

(e) $Re_\tau = 180$ (f) $Re_\tau = 395$

Figure 8: Profiles of the premultiplied budget terms in the spectral transport equation of Reynolds normal stresses calculated at the peak position of $\langle w'w' \rangle^+$ along the semi-major axis for each test case (i.e, at a distance from the wall of $x^+ = 16.7$ and 15.4 for the cases of $Re_\tau = 180$ and 395, respectively). All terms are non-dimensionalized by u_τ^5/ν^2.

CONCLUSION

Turbulent transport of Reynolds normal stresses in elliptical pipe flow has been studied in both physical and spectral spaces using DNS at $Re_\tau = 180$ and 395. The present study extends current understanding of turbulence in non-circular pipe flows and aims to provide new insights into spectral transport processes.

In physical space, all Reynolds normal stress components increase in magnitude along the semi-major axis with an increasing Reynolds number, with their peak values shifting toward the wall. In examining the budget terms of the Reynolds stress transport equation, it is interesting to observe opposite behaviors of the streamwise and vertical pressure-strain terms (Π_{33} and Π_{22}, respectively), clearly indicating a redistribution of TKE between these two Reynolds normal stress components.

In spectral space, the premultiplied energy spectra shift toward smaller streamwise wavelengths as the Reynolds number increases. The spectral budgets reveal that the inter-scale transport term $\widetilde{T}_{33}$ promotes a forward cascade from large to small scales. Interestingly, $\widetilde{T}_{22}$ exhibits inverse energy transfer from small to large scales, highlighting anisotropic and component-dependent energy transfer at the end of the semi-major axis.

Acknowledgment

The authors would like to thank the University of Manitoba for access to the GREX supercomputing and storage facilities. The spectral-element code developed by Blackburn *et al.* (2019) was critical for generating the DNS data. Their contributions are greatly appreciated.

REFERENCES

Blackburn, H.M., Lee, D., Albrecht T. & Singh, J. Semtex: a spectral element Fourier solver for the incompressible Navier-Stokes equations in cylindrical or Cartesian coordinates. *Comput. Phys. Commun.* **140**, 27–44, 2019.

Cain, D. & Duffy, J. An Experimental Investigation of Turbulent Flow in Elliptical Ducts. *Int. J. Mech. Sci.* **13**, 451–459, 1971.

Karniadakis, G. E., Isreali, M., & Orszag, S. A. High-order splitting methods for the incompressible Navier-Stokes equations. *J. Comp. Phys.* **97**(2), 414–443, 1991.

Kawata, T. & Alfredsson, P. H., Inverse interscale transport of the Reynolds Shear Stress in Plane Couette Turbulence. *Phys. Rev. Lett.* **120**, 244501, 2018.

Karniadakis, G. E. & Sherwin, S. Spectral/hp Element Methods for Computational Fluid Dynamics. *Oxford University Press*, 2005.

Lee, M. & Moser, R. D. Spectral analysis of the budget equation in turbulent channel flows at high Reynolds number. *J. Fluid Mech.* **860**, 886–938, 2019.

Lumley, J. L. Spectral energy budget in wall turbulence. *Phys. Fluids* **7**(2), 190–196, 1964.

Mizuno, Y. Spectra of energy transport in turbulent channel flows for moderate Reynolds numbers. *J. Fluid Mech.* **805**, 171–187, 2016.

Mansour, N. N., Kim, J. & Moin, P. Reynolds-stress and dissipation-rate budgets in a turbulent channel flow. *J. Fluid Mech.* **194**, 15–44, 1988.

Nikitin, N. & Yakhot, A. Direct numerical simulation of turbulent flow in elliptical ducts *J. Fluid Mech.* **532**, 141–164, 2005.

Opperman, T. C., Zhang, Z.-P., Rosas, R. H. & Wang, B.-C. Effects of aspect ratio on turbulent elliptical pipe flow and structures. *Phys. Fluids*, **37**(10) 105121, 2025.

Rosas, R. H., Zhang, Z.-P. & Wang, B.-C. Direct numerical simulation of turbulent elliptical pipe flow under system rotation about the major axis. *Phys. Rev. Fluids* **6**, 084609, 2021.

Rosas, R. H. & Wang, B.-C. Direct numerical simulation of turbulent heat transfer in an elliptical pipe flow subjected to system rotation about the major axis. *Int. J. Heat Mass Transf.* **184**, 122230, 2022.

Tachie, M. S., Xiong, W.-J. & Wang, B.-C. DNS of turbulent flow in a square duct roughened by longitudinal ribs. *Phys. Rev. Fluids* **10**, 114604, 2025.

Voronova, T. V. & Nikitin, N. V. Direct numerical simulation of the turbulent flow in an elliptical pipe. *Comput. Math. Math. Phys.* **46**, 1378–1386, 2006.

Voronova, T. V. & Nikitin, N. V. Results of direct numerical simulation of turbulent flow in a pipe of elliptical cross-section. *Fluid Dyn.* **42**, 201–211, 2007.

Xiong, W.-J., Xu, J., Wang, B.-C. & Mahmoodi-Jezeh, S. V. Direct numerical simulation of turbulent convection in a channel roughened with circular-arc ribs. *Int. J. Heat Fluid Flow* **104**, 109213, 2023.

Xiong, W.-J., Xu, J., Wang, B.-C. & Mahmoodi-Jezeh, S. V. Direct numerical simulation of turbulent heat transfer in a channel with circular-arc ribs mounted on one wall. *Int. J. Heat Fluid Flow* **110**, 109638, 2024.

Xiong, W.-J., Xu, J., Opperman, T. C. & Wang, B.-C. Spectral analysis of turbulence energy transport in a channel mounted with circular-arc ribs. *J. Fluid Mech.* **1025**, A33, 2025.

Yang, Z., Deng, B. Q., Wang, B.-C. & Shen, L. Sustaining mechanism of Taylor-Görtler-like vortices in a streamwise-rotating channel flow. *Phys. Rev. Fluids* **5**(4), 044601, 2020.

Zhang, Z.-P. & Wang, B.-C. Direct numerical simulation of turbulent flow and structures in a circular pipe subjected to axial system rotation. *J. Fluid Mech.*, **1000** A1, 2024.

APPENDIX A: TRANSPORT EQUATION OF REYNOLDS STRESSES

In the physical space, the transport equation for Reynolds stresses in a statistically-stationary fully-developed flow is expressed as (Mansour *et al.*, 1988)

$$\frac{\partial \langle u_i' u_j' \rangle}{\partial t} = H_{ij} + P_{ij} + \Pi_{ij} + \varepsilon_{ij} + D_{ij}^t + D_{ij}^p + D_{ij}^v = 0 \quad , \tag{6}$$

where H_{ij}, P_{ij}, Π_{ij}, ε_{ij}, D_{ij}^t, D_{ij}^p, and D_{ij}^v are the convection, turbulent production, pressure-strain, viscous dissipation, turbulent diffusion, pressure diffusion, and viscous diffusion terms, respectively. These terms are defined as

$$H_{ij} = -\langle u_k \rangle \frac{\partial \left\langle u_i' u_j' \right\rangle}{\partial x_k} \quad , \tag{7}$$

$$P_{ij} = -\langle u_i' u_k' \rangle \frac{\partial \langle u_j \rangle}{\partial x_k} - \langle u_j' u_k' \rangle \frac{\partial \langle u_i \rangle}{\partial x_k} \quad , \tag{8}$$

$$\Pi_{ij} = \frac{1}{\rho} \left\langle p' \left(\frac{\partial u_i'}{\partial x_j} + \frac{\partial u_j'}{\partial x_i} \right) \right\rangle \quad , \tag{9}$$

$$\varepsilon_{ij} = -2\nu \left\langle \frac{\partial u_i'}{\partial x_k} \frac{\partial u_j'}{\partial x_k} \right\rangle \quad , \tag{10}$$

$$D_{ij}^t = -\frac{\partial \left\langle u_i' u_j' u_k' \right\rangle}{\partial x_k} \quad , \tag{11}$$

$$D_{ij}^p = -\frac{1}{\rho} \frac{\partial}{\partial x_k} \left(\langle p' u_j' \rangle \delta_{ik} + \langle p' u_i' \rangle \delta_{jk} \right) \quad , \tag{12}$$

$$D_{ij}^v = \nu \frac{\partial^2 \left\langle u_i' u_j' \right\rangle}{\partial x_k \partial x_k} \quad . \tag{13}$$

APPENDIX B: TRANSPORT EQUATION OF VELOCITY SPECTRA

In the spectral space, the transport equation for the velocity-spectrum tensor in a statistically-stationary fully-developed flow is given by (Lee & Moser, 2019; Xiong *et al.*, 2025)

$$\frac{\partial \overline{\widehat{u_i'}^* \widehat{u_j'}}}{\partial t} = \widetilde{H}_{ij} + \widetilde{P}_{ij} + \widetilde{T}_{ij} + \widetilde{\Pi}_{ij} + \widetilde{\varepsilon}_{ij} + \widetilde{D}_{ij}^t + \widetilde{D}_{ij}^p + \widetilde{D}_{ij}^v = 0 \quad , \tag{14}$$

where $\widetilde{H}_{ij}$, $\widetilde{P}_{ij}$, $\widetilde{T}_{ij}$, $\widetilde{\Pi}_{ij}$, $\widetilde{\varepsilon}_{ij}$, $\widetilde{D}_{ij}^t$, $\widetilde{D}_{ij}^p$, and $\widetilde{D}_{ij}^v$ are the convection, turbulent production, inter-scale transport, pressure-strain, viscous dissipation, turbulent diffusion, pressure diffusion, and viscous diffusion terms, respectively. These terms are defined as

$$\widetilde{H}_{ij} = \mathrm{Re}\left\{ -\langle u_1 \rangle \frac{\partial \overline{\widehat{u_i'}^* \widehat{u_j'}}}{\partial x_1} - \langle u_2 \rangle \frac{\partial \overline{\widehat{u_i'}^* \widehat{u_j'}}}{\partial x_2} \right\} \quad , \tag{15}$$

$$\widetilde{P}_{ij} = \mathrm{Re}\left\{ -\overline{\widehat{u_k'}^* \widehat{u_j'}} \frac{\partial \langle u_i \rangle}{\partial x_k} - \overline{\widehat{u_k'} \widehat{u_i'}^*} \frac{\partial \langle u_j \rangle}{\partial x_k} \right\} \quad , \tag{16}$$

$$\begin{aligned} \widetilde{T}_{ij} = \mathrm{Re}\Bigg\{ & -\overline{\widehat{u_j'} \frac{\partial \widehat{u_i' u_1'}^*}{\partial x_1}} - \overline{\widehat{u_i'}^* \frac{\partial \widehat{u_j' u_1'}}{\partial x_1}} - \overline{\widehat{u_j'} \frac{\partial \widehat{u_i' u_2'}^*}{\partial x_2}} - \overline{\widehat{u_i'}^* \frac{\partial \widehat{u_j' u_2'}}{\partial x_2}} \\ & + \frac{1}{2} \left(\frac{\partial \overline{\widehat{u_i' u_1'}^* \widehat{u_j'}}}{\partial x_1} + \frac{\partial \overline{\widehat{u_i' u_2'}^* \widehat{u_j'}}}{\partial x_2} + \frac{\partial \overline{\widehat{u_j' u_1'} \widehat{u_i'}^*}}{\partial x_1} + \frac{\partial \overline{\widehat{u_j' u_2'} \widehat{u_i'}^*}}{\partial x_2} \right) \\ & - \mathrm{i} k_3 \left(\overline{\widehat{u_i'}^* \widehat{u_j' u_3'}} - \overline{\widehat{u_j'} \widehat{u_i' u_3'}^*} \right) \Bigg\} \quad , \end{aligned} \tag{17}$$

$$\begin{aligned} \widetilde{\Pi}_{ij} = \mathrm{Re}\Bigg\{ & \frac{1}{\rho} \Bigg(\overline{\widehat{p'}^* \frac{\partial \widehat{u_j'}}{\partial x_1}} \delta_{i1} + \overline{\widehat{p'}^* \frac{\partial \widehat{u_j'}}{\partial x_2}} \delta_{i2} + \overline{\widehat{p'} \frac{\partial \widehat{u_i'}^*}{\partial x_1}} \delta_{j1} + \overline{\widehat{p'} \frac{\partial \widehat{u_i'}^*}{\partial x_2}} \delta_{j2} \\ & + \mathrm{i} k_z \left(\overline{\widehat{p'}^* \widehat{u_j'}} \delta_{i3} - \overline{\widehat{p'} \widehat{u_i'}^*} \delta_{j3} \right) \Bigg) \Bigg\} \quad , \end{aligned} \tag{18}$$

$$\widetilde{\varepsilon}_{ij} = \mathrm{Re}\left\{ -2\nu \overline{\frac{\partial \widehat{u_i'}^*}{\partial x_1} \frac{\partial \widehat{u_j'}}{\partial x_1}} - 2\nu \overline{\frac{\partial \widehat{u_i'}^*}{\partial x_2} \frac{\partial \widehat{u_j'}}{\partial x_2}} - 2\nu k_z^2 \overline{\widehat{u_i'}^* \widehat{u_j'}} \right\} \quad , \tag{19}$$

$$\begin{aligned} \widetilde{D}_{ij}^t = \mathrm{Re}\Bigg\{ & -\frac{1}{2} \Bigg(\frac{\partial \overline{\widehat{u_i' u_1'}^* \widehat{u_j'}}}{\partial x_1} + \frac{\partial \overline{\widehat{u_i' u_2'}^* \widehat{u_j'}}}{\partial x_2} \\ & + \frac{\partial \overline{\widehat{u_j' u_1'} \widehat{u_i'}^*}}{\partial x_1} + \frac{\partial \overline{\widehat{u_j' u_2'} \widehat{u_i'}^*}}{\partial x_2} \Bigg) \Bigg\} \quad , \end{aligned} \tag{20}$$

$$\begin{aligned} \widetilde{D}_{ij}^p = \mathrm{Re}\Bigg\{ & -\frac{1}{\rho} \Bigg(\frac{\partial \overline{\widehat{p'}^* \widehat{u_j'}}}{\partial x_1} \delta_{i1} + \frac{\partial \overline{\widehat{p'}^* \widehat{u_j'}}}{\partial x_2} \delta_{i2} \\ & + \frac{\partial \overline{\widehat{p'} \widehat{u_i'}^*}}{\partial x_1} \delta_{j1} + \frac{\partial \overline{\widehat{p'} \widehat{u_i'}^*}}{\partial x_2} \delta_{j2} \Bigg) \Bigg\} \quad , \end{aligned} \tag{21}$$

$$\widetilde{D}_{ij}^v = \mathrm{Re}\left\{ \nu \left(\frac{\partial^2 \overline{\widehat{u_i'}^* \widehat{u_j'}}}{\partial x_1^2} + \frac{\partial^2 \overline{\widehat{u_i'}^* \widehat{u_j'}}}{\partial x_2^2} \right) \right\} \quad . \tag{22}$$